Stable sodium-sulfur electrochemistry enabled by phosphorus-based complexation

Chuanlong Wang[a,1], Yue Zhang[b,1], Yiwen Zhang[a], Jianmin Luo[a], Xiaofei Hu[a], Edward Matios[a], Jackson Crane[b], Rui Xu[b], Hai Wang[b,2], and Weiyang Li[a,2]

[a]Thayer School of Engineering, Dartmouth College, Hanover, NH 03755; and [b]Department of Mechanical Engineering, Stanford University, Stanford, CA 94305

Edited by Alexis T. Bell, University of California, Berkeley, CA, and approved October 29, 2021 (received for review September 5, 2021)

A series of sodium phosphorothioate complexes are shown to have electrochemical properties attractive for sodium-sulfur battery applications across a wide operating temperature range. As cathode materials, they resolve a long-standing issue of cyclic liquid–solid phase transition that causes sluggish reaction kinetics and poor cycling stability in conventional, room-temperature sodium-sulfur batteries. The cathode chemistry yields 80% cyclic retention after 400 cycles at room temperature and a superior low-temperature performance down to −60 °C. Coupled experimental characterization and density functional theory calculations revealed the complex structures and electrochemical reaction mechanisms. The desirable electrochemical properties are attributed to the ability of the complexes to prevent the formation of solid precipitates over a fairly wide range of voltage.

sodium chemistry | phosphorothioates | phosphorus pentasulfide | semisolid batteries

Sodium batteries are promising alternatives to lithium-ion batteries in energy storage applications (1, 2). As an alkali metal and being substantially more naturally abundant than lithium, sodium shares many of the similar chemical and physical properties as lithium (2). With a lower first ionization energy than lithium (495.8 versus 520.2 kJ mol^{-1}), sodium can present improved chemical and electrochemical reactivity over lithium (3). Although simply replacing lithium with sodium in conventional lithium-ion batteries is not a viable solution because of deteriorating electron transfer in intercalation cathodes, sodium is more attractive when leveraged with other battery chemistries owing to its unique redox reactions (4, 5).

Among emerging high-capacity cathode materials, sulfur is a prime candidate because of its capability to enable multielectron redox reactions (4–10). Pairing a sulfur cathode with a metallic sodium anode forms a sodium-sulfur battery that undergoes a two-electron transfer process, yielding a theoretical specific energy of 1,274 Wh per kg of sulfur (6–10), which is substantially higher than that of intercalation-based chemistry (<400 Wh kg^{-1}) (4, 5). Compared to the lithium-sulfur battery, a sodium-sulfur battery can be made from low-cost materials with little to no geographical constraint, thus offering additional advantages, especially for large-scale energy storage applications (6–10). Yet, key challenges remain in realizing a high-performance sodium-sulfur battery. Critical problems include the formation of undesirable intermediates (e.g., long-chain polysulfides) and irreversible precipitation of solid products (e.g., short-chain sulfides with poor electronic/ionic conductivity) (4–13), leading to sluggish reaction kinetics, low practical capacity and Coulombic efficiency, and more importantly, extremely poor cycle life. To tackle these problems, various structural and compositional developments on sulfur-containing cathodes (11, 12), including sulfur-based composites and sodium polysulfide/sulfide, have been evaluated, showing promising results. Nevertheless, the intrinsic cyclic liquid–solid phase transitions that impair the long-term stability of the battery chemistry remains unresolved using these earlier approaches.

In the current work, we introduce phosphorus into sodium and sulfur redox reactions to enable a battery chemistry that prevents cyclic liquid–solid phase transitions. Our idea was inspired by the recent development of glassy sulfide solid electrolytes (14–17), in which a sulfide network establishes strongly cross-linked macromolecular chains to facilitate glass formation. We find that the interactions between sodium polysulfide (Na_2S_x) and phosphorus pentasulfide (P_2S_5) yield tetrahedral phosphorus (V) centers, which can effectively bridge polysulfide chains to yield a series of previously unexplored sodium phosphorothioate complexes. As battery cathode materials, these complexes are able to anchor polysulfides, long and short, via phosphorus-sulfur (P-S) coordination or covalent bonding, thus preventing undesirable products from forming during battery cycling and effectively and significantly extending battery cycle life.

Results from the present work show that for a series of sodium phosphorothioate complexes we synthesized, those with longer S_x chains ($6 \leq x \leq 8$) possess electrochemical reactivities superior to the conventional sodium-sulfur battery chemistry, especially in extending cycle life and maintaining high Coulombic efficiency. When used as a catholyte (a liquid-phase cathode) with a sodium anode, a proof-of-concept battery delivered 80% cyclic retention over 400 cycles, an average Coulombic

Significance

Beyond lithium-ion technologies, sodium-sulfur batteries stand out because of their multielectron redox reactions and high theoretical specific energy (1,274 Wh per kg of sulfur). They hold the potential of overcoming the capacity limitation of intercalation-based chemistry (<400 Wh kg^{-1}). Major challenges in realizing this potential lie in the formation of undesirable intermediates, irreversible precipitation of solid products, and hence, poor battery cycle life. This work presents a series of sodium phosphorothioate complexes that show superior battery performance at ambient and reduced temperatures. They offer great promise for enabling sodium-based energy storage systems with wide-ranging temperature operability. The coupled experimental characterization and theoretical analysis are valuable for guiding complex synthesis, experimental design, and data interpretation.

Author contributions: C.W., Yue Zhang, H.W., and W.L. designed research; C.W. and Yue Zhang performed research; C.W., Yue Zhang, Yiwen Zhang, J.L., X.H., and E.M. contributed new reagents/analytic tools; C.W., Yue Zhang, H.W., and W.L. analyzed data; and C.W., Yue Zhang, J.C., R.X., H.W., and W.L. wrote the paper.

The authors declare no competing interest.

This article is a PNAS Direct Submission.

[1]C.W. and Yue Zhang contributed equally to this work.

[2]To whom correspondence may be addressed. Email: haiwang@stanford.edu or weiyang.li@dartmouth.edu.

This article contains supporting information online at http://www.pnas.org/lookup/suppl/doi:10.1073/pnas.2116184118/-/DCSupplemental.

Published December 2, 2021.

efficiency >95% over 200 cycles, and an initial capacity of 440 mAh per gram of active sulfur (924 Wh per kg based on a discharge potential of 2.10 V) under a relatively high charge/discharge rate of 0.5C at room temperature (see *SI Appendix, Methods* for active sulfur definition). In comparison, the same battery using conventional sodium sulfide chemistry delivered 350 mAh per gram of active sulfur (682 Wh per kg based on a discharge potential of 1.95 V) under comparable conditions, but it operated at <22% initial Coulombic efficiency for <50 cycles before completely losing its storage capacity. Low-temperature battery performance characterization demonstrates that complexation enables facile electrochemistry while still minimizing undesirable cyclic liquid–solid phase transitions down to −60 °C. To enable complex chemical structure design, we conducted coupled experimental characterization using Raman spectroscopy and NMR spectroscopy and theoretical density functional theory (DFT) calculations to explore the molecular structures of the complexes and their thermochemistry and the underlying electrochemical reaction mechanisms.

Results

Molecular Design. Sodium phosphorothioates were synthesized by reacting sodium sulfide (Na_2S), P_2S_5 and sulfur powders in diethylene glycol dimethyl ether (diglyme) (see *SI Appendix, Methods*). The reaction products are denoted as mP_2S_5-nNa_2S_x ($1 \le x \le 8$) hereafter, and their compositions may be tailored in two separate dimensions to enable distinctive solubility and electrochemical properties—the S_x chain length (x) and the P_2S_5/Na_2S_x molar ratio (m:n)—thus enabling a semisolid sodium battery concept illustrated in Fig. 1*A*. In it, a catholyte (mP_2S_5-nNa_2S_x, *yellow*)–infiltrated carbon fiber paper (*gray*) serves as the cathode and a piece of pretreated metallic sodium (*gray*) coated with passivation layer (*cyan*) serves as the anode.

Various S_x chain lengths (x = 1, 2, 3, 4, 6, and 8) and P_2S_5/Na_2S_x ratios (m:n = 1:2, 2:3, 1:1, 3:2, and 2:1) were evaluated in Fig. 1*B*. The catholytes are all dissolved in diglyme with 20 wt% (solid-to-liquid) loading and prepared in an argon-filled glove box by stirring without heating. In diglyme, the sodium phosphorothioates are readily distinguished by their visual appearances. Without P_2S_5, the shorter-chain Na_2S_x ($x \le 3$) complexes are insoluble, Na_2S_4 shows a limited dissolution (<20 wt%), and Na_2S_6 and Na_2S_8 can be fully dissolved, with the resulting solutions dark red-brown in color. With P_2S_5 added at a molar ratio (m:n) of 1:1, all Na_2S_x compounds complex well in diglyme and produce transparent and homogeneous solutions regardless of S_x chain length. The colors range from orange to light yellow to slightly deeper yellow as the S_x chain length increases. Systems of mP_2S_5-nNa_2S_8 with m:n ratios between 1:2 and 2:1 are investigated (Fig. 1*B*, bottom row). Homogeneous solutions with long sulfide chains (x = 8) are also formed in the m:n range of 2:3 to 3:2, though they exhibit distinctive color differences (m:n = 2:3: dark red; 1:1: yellow; 3:2: deeper yellow). Neither the m:n = 1:2 nor 2:1 ratio gives soluble results.

Characterizations of mP_2S_5-nNa_2S_x Complexes. Following the approach commonly used in studies of glassy phosphorothioate materials (13, 14, 18, 19), we classify the nature of the P_2S_5 derivatives in terms of their P^s short-range orders (SROs) identifiable via the ^{31}P chemical shifts in an NMR observation. Each of the SROs corresponds to a local phosphorus bonding structure, where the superscript s denotes the number of bridging sulfur atoms that a particular phosphorus atom is bonded with. Five major chemical shifts were identified by NMR for the as-prepared soluble mP_2S_5-nNa_2S_x solutions: 127, 118, 63, 49, and 30 ppm (Fig. 1*C*). DFT calculations identified the expected NMR chemical shift for each SRO, and based on these calculations, the experimental shifts are assigned to the P^0, P^2, P^3, $P^{2'}$ and $P^{2''}$ SROs, respectively (*SI Appendix*, Table S2). P^3, P^2, and $P^{2'}$ are the dominating structures for the longer S_x chains (x = 4, 6, 8), while P^0 and $P^{2''}$ are mainly associated with the shorter S_x chains (x = 1, 2). In the P^3 SRO, all three single-bonded sulfur atoms branch, and in P^2 and $P^{2'}$, two sulfur atoms and one sulfur branch, respectively; all of these SROs can enable cross-linking. Interestingly, the P^2 resonance disappears in the $3P_2S_5$-$2Na_2S_8$ complex, possibly because of excessive P_2S_5 interaction with P^2 (linear connectivity) to form P^3 (higher-order network connectivity) (14–17). Except for P^3, no NMR resonance is observed in $2P_2S_5$-$3Na_2S_8$, which may be due to network destruction by excess Na_2S_8. The P^0 SRO is associated only with the Na_2S and Na_2S_2 complexes with no cross-linking in any way. In what follows, we will focus our discussion on stoichiometric P_2S_5-Na_2S_x complexes, even though additional benefits may result from different m:n ratios.

Raman profiles (Fig. 1*D*) confirm the presence of SROs and S_x chains in complexes and reveal their chemical interactions. The characteristic peaks of the precursors (*SI Appendix*, Fig. S1) disappear, and new peaks arise upon complexation. The 388 and 418 cm^{-1} peaks indicate the $P^{2''}$ SRO, and the 482 cm^{-1} peak can be ascribed to the -S-S- symmetric in S_x chains bonded by other SROs (14–17, 19). In the P_2S_5-$Na_2S_{x\ge2}$ profiles, the 200–215 cm^{-1} band indicates P^2 and/or P^3 SROs, and the 386 and 493 cm^{-1} peaks reveal the modes in P^2. For P_2S_5-Na_2S_x (x = 4, 6, and 8), two more peaks at 239 and 258 cm^{-1} are observed, both of which are associated with the $P^{2'}$ SRO (14–17). The peak at ~575 cm^{-1} is assigned to the T_2 asymmetric stretching in the tetrahedral structure of all SROs (14–18), which shifts to lower energies as the S_x chain length increases, suggesting the interconnection between the chains and SRO units (19). The 325 cm^{-1} hump in the Raman is associated with diglyme solvent, as shown in *SI Appendix*, Fig. S1.

Complexation does not appear to be sensitive to the solvent used. Among the solvents tested [diglyme, 1,2-dimethoxyethane (DME) and tetrahydrofuran (THF)], we found no evidence of solvent reaction with the complex or its precursors (see the ^1H-NMR profiles in *SI Appendix*, Figs. S2–S4). The ^{31}P-NMR profiles (*SI Appendix*, Fig. S5) show similar resonances of P_2S_5-Na_2S_8 in DME, THF, and diglyme, with only minor differences attributable to solvent polarities (diglyme > THF > DME). Also, the ^{31}P-NMR spectrum (*SI Appendix*, Fig. S6) shows the P_2S_5-Na_2S_8 complex to be stable after storage for 30 days in diglyme.

Complexation Mechanism. Phosphorus is strongly oxygenophilic, enabling it to bond with sulfur anions. In fact, the most stable structure of P_2S_5 is its dimer (P_4S_{10}). For a sufficiently long S_x chain ($x \ge 4$), the initial complexation may be identified from a joint consideration of NMR and Raman characterizations and DFT calculations as a four-centered reaction process depicted in Fig. 1*E*. Upon the addition of two Na_2S_x to each P_4S_{10}, internal isomerization or the opening of the six-membered ring produces a prototypical unit structure, as shown in the lower-left corner of Fig. 1*E*. In this subfigure, all relevant SROs (i.e., P^3, P^2, and $P^{2'}$) are labeled. The P^0 and $P^{2''}$ SROs are excluded from the complexation mechanism, as they are absent in P_2S_5-$Na_2S_{x>2}$ complexes. One end of the two available NaS_x chains is anchored on the P-S backbone, and the other end can repeat similar reactions with other P_4S_{10} molecules (not drawn), leading to interconnectivity, cross-linking, and higher-order complex formation (see, e.g., a possible dimerization mechanism in *SI Appendix*, Fig. S7). The S-chain flexibility enables a glassy material–like structure suitable for ion transport (14–17). Clearly, longer S_x chains favor intramolecular isomerization that forms $P^{2'}$ and intermolecular bonding, whereas shorter S_x chains favor intermolecular bonding only, which forms P^2 preferably, in agreement with the relative abundances of $P^{2'}$ and P^2 SROs observed in NMR as a function of the S_x chain length (Fig. 1*C*).

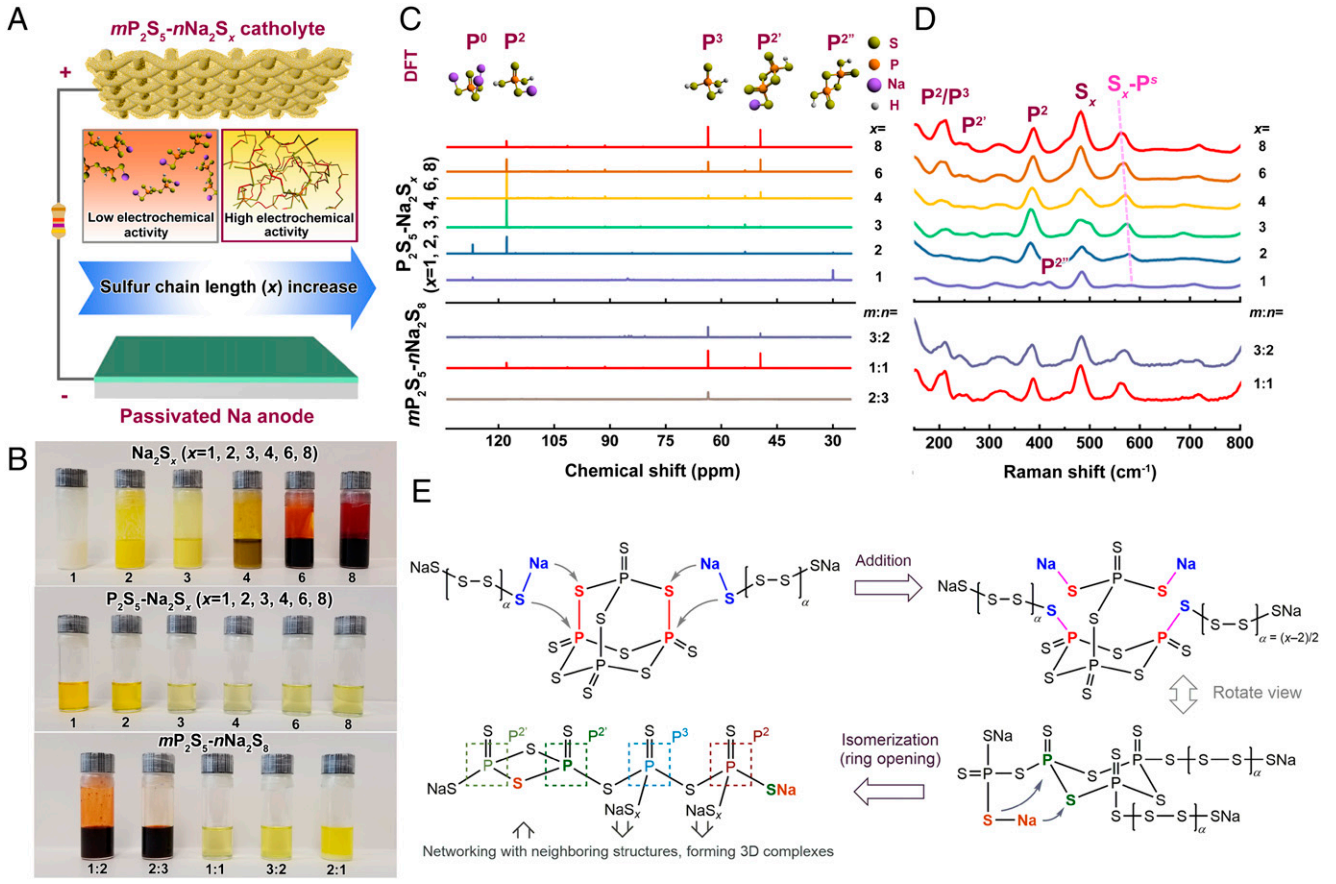

Fig. 1. Illustration of mP_2S_5-nNa_2S_x complex battery chemistry, characterizations of mP_2S_5-nNa_2S_x complexes, and proposed complexation mechanism. (*A*) The sodium battery structures anchored on mP_2S_5-nNa_2S_x complexes on the catholyte side. (*B*) Photos of Na_2S_x (*top row*); P_2S_5-Na_2S_x complexes for x = 1, 2, 3, 4, 6, 8 (*middle row*); and mP_2S_5-nNa_2S_8 complexes for m:n = 1:2, 2:3, 1:1, 3:2, 2:1. (*C*) ^{31}P-NMR spectra of P_2S_5-Na_2S_x (x = 1, 2, 3, 4, 6, 8) and mP_2S_5-nNa_2S_8 (m:n = 2:3, 1:1, 3:2) in diglyme with the corresponding P^s (s = 0, 2, 2′, 2″, 3) short-range order structure positions assigned based on DFT calculations. (*D*) Raman analyses of the P_2S_5-Na_2S_x (x = 1, 2, 3, 4, 6, 8) and mP_2S_5-nNa_2S_8 (m:n = 1:1, 3:2) complexes in diglyme. (*E*) Initial complexation of P_4S_{10} and Na_2S_x at 1:2 molar ratio (1:1 ratio in P_2S_5-Na_2S_x), leading to the formation of P^2, $P^{2'}$, and P^3 as the key SROs observed by ^{31}P-NMR and Raman (the subscript *a* denotes the number of S-S bonds).

Electrochemical Reaction Mechanism. Polysulfide chain anchoring on the phosphorothioate network is key to the current battery chemistry, as the DFT calculations revealed. In Fig. 2*A*, we illustrate two idealized electrochemical reactions that are characterized by the breakage/addition of the S-S bond in a NaS_2-S_{x-2}- chain in a two-electron discharging/charging process. In reaction 1, the NaS_2^- anion produced by the bond breakage combines with Na^+, forming Na_2S_2, which is then accommodated in the network by forming a pair of coordination bonds with a pair of phosphorus atoms (20). The coordination reaction is the key to preventing the formation of insoluble products. Reaction 2 features the $P^{2'}$-to-P^2 conversion, in which the NaS_2^- anion bonds with phosphorus following the S-P bond breakage. The discharge reaction products are again accommodated on the network, and the Na-S_{x-2}- group is available for further reduction. In these idealized reactions, each P_4S_{10} unit can accommodate up to seven Na_2S_2 (see *SI Appendix*, Fig. S8 and the explanation given in the figure caption). Hence, for the stoichiometric P_2S_5-Na_2S_8 complex, the fully discharged state would have only one excess Na_2S_2 that cannot be accommodated by the complex. If, however, the end product is Na_2S, 11 Na_2S can be fully accommodated by the complex, and five Na_2S are excess and cannot be accommodated. The actual reaction process and hence the products formed are more complex than the limiting cases just discussed.

Proof-of-concept battery cells were constructed using P_2S_5-Na_2S_x (x = 1, 2, 3, 4, 6, and 8) as the catholytes and pretreated sodium metal as the anode. Sodium metal was pretreated using a passivation solution as reported in our previous study (13), which prevents the anode from directly contacting electrolyte and polysulfides (*SI Appendix*, Section S1). Cyclic voltammetry (CV) curves presented in Fig. 2*B* show well-defined oxidation and reduction peaks and reversible redox reactions for P_2S_5-Na_2S_x with x = 3, 4, 6, and 8. P_2S_5-Na_2S and P_2S_5-Na_2S_2 exhibit very low electrochemical activities. Further investigations were focused on P_2S_5-Na_2S_8 because of its high activity. For comparison, reference cells were prepared using Na_2S_8 (without P_2S_5 complexation) as the catholyte. Under comparable conditions, the P_2S_5-Na_2S_8 cell exhibits more pairs of redox peaks and enhanced electrochemical reaction kinetics as compared to the Na_2S_8 cell (*SI Appendix*, Figs. S9 and S10).

The P_2S_5-Na_2S_8 catholyte cell shows major activities at 2.23, 2.11, 1.93, and 1.70 V on the CV profile (Fig. 2*B*). The Raman spectra (Fig. 2*D*) suggest that from 2.4 to 1.8 V, the reaction involves mainly the reduction of the catholyte from S_8^{2-} to $S_3^{\cdot-}$. Below 1.8 V and continuing to 1.2 V, the reduction eventually produces S_2^{2-}. The spectra also show the $P^{2'}$ to P^2 transformation during discharge in the P_2S_5-Na_2S_8 cell, in agreement with the reaction mechanism (Reaction 2) illustrated in Fig. 2*A*. Complexation enables the accommodation of the S_2^{2-} and even

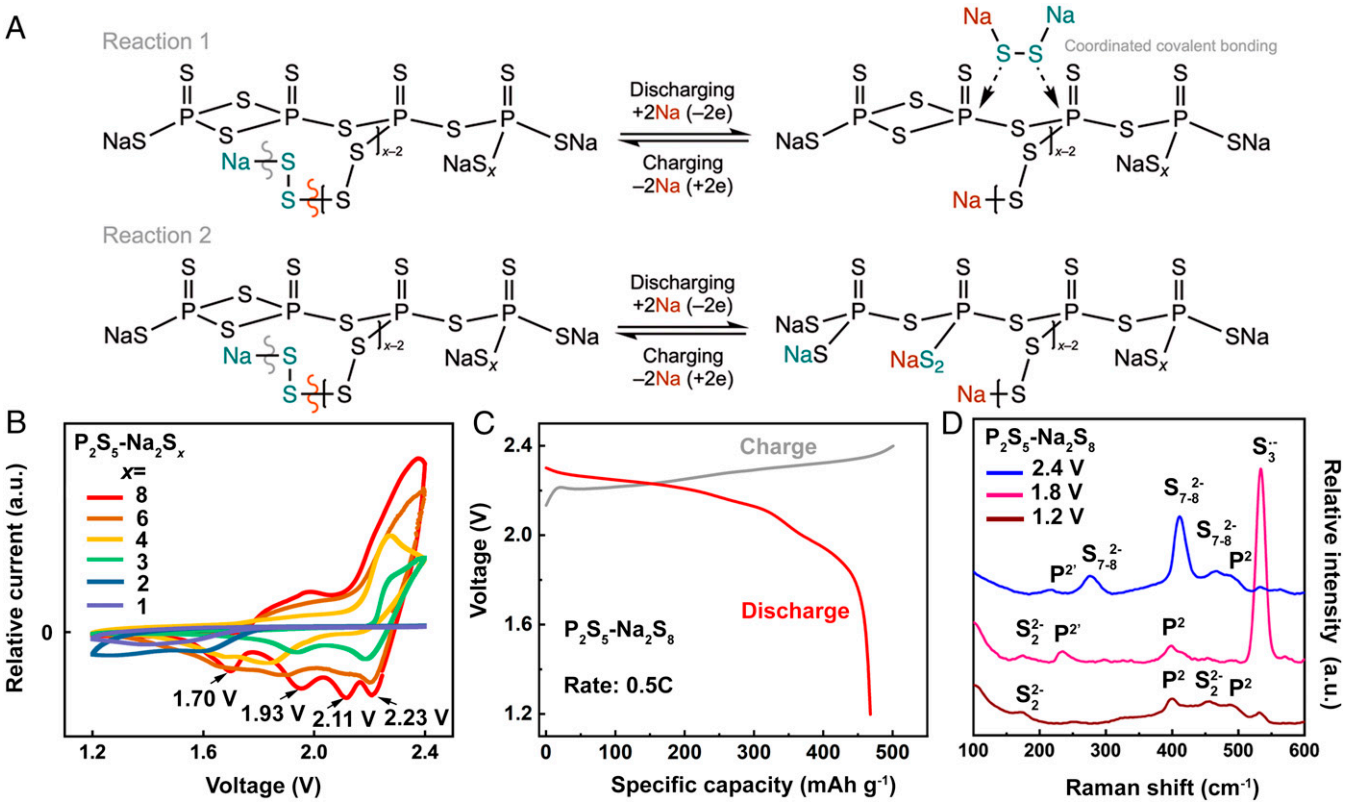

Fig. 2. Electrochemical reaction mechanisms investigation. (*A*) Reaction mechanisms: Reaction 1 features discharging, involving the removal of S_2^{2-} from an initial S_x chain ($x \geq 4$) and the formation of Na_2S_2 that can be coordinated with the complex; reaction 2 features discharging through the opening of the four-membered ring, followed by S_2^{2-} addition to the P atom. (*B*) CV for cells comprising P_2S_5-Na_2S_x (x = 1, 2, 3, 4, 6, 8) catholytes and a passivated sodium anode at a scan rate of 0.1 mV s^{-1} at room temperature (experimental results are scaled to identical sulfur molar concentrations in Na_2S_x). (*C*) Typical room-temperature galvanostatic charge (*gray line*)–discharge (*red line*) curves of the P_2S_5-Na_2S_8 catholyte cell at 0.5C (1C = 1,675 mA g^{-1}) over the voltage range from 1.2 V to 2.4 V. (*D*) Raman spectra of the P_2S_5-Na_2S_8 catholyte charged to the end voltage of 2.4 V and discharged to end voltages of 1.8 V and 1.2 V, respectively, during cycling at 0.5C (1C = 1,675 mA g^{-1}). a.u., arbitrary unit.

S_1^{2-} species into the complex as discussed before, thus maintaining the electrochemical reversibility. For Na_2S_8, we observed major electrochemical activities at around 2.2 and 1.7 V and a minor activity region near 1.9 V from the CV profile (*SI Appendix*, Figs. S9 and S12). Unlike the P_2S_5-Na_2S_8 cell, the Na_2S_8 cell produced solid sulfur (S_8) and a substantial amount of untransformed $S_3^{\cdot-}$ (see the Raman profile of *SI Appendix*, Fig. S13), both of which are indicative of the undesirable phase transition and electrochemical irreversibility of Na_2S_8. Not surprisingly, galvanostatic characterization showed that the P_2S_5-Na_2S_8 cell has a steady charge curve corresponding to a Coulombic efficiency of 93% (Fig. 2*C*). Under comparable condition, the Na_2S_8 cell gives a much smaller Coulombic efficiency (22%) (*SI Appendix*, Fig. S12). The P_2S_5-Na_2S_8 complex yielded a higher discharge potential than Na_2S_8 (2.10 V versus 1.95 V). As importantly, the complex-based chemistry did not show a significant reduction in discharge capacity. We observed an initial capacity of 228 mAh per gram of complex material (P_2S_5-Na_2S_8) versus 292 mAh per gram of Na_2S_8 without complexation. On an active sulfur basis (see *SI Appendix*, *Methods* for active sulfur definition), these capacity values correspond to 468 mAh g^{-1} for the P_2S_5-Na_2S_8 complex, larger than that of the Na_2S_8 cell at 345 mAh g^{-1}, as one would expect from the molecular-weight difference.

The electrochemical activity of P_2S_5-Na_2S_x depends on the length of the S_x chain, both as a catholyte reactant and the intermediates during catholyte reduction. In general, a longer sulfur chain enables more electron transfers and therefore a higher initial electrochemical potential. DFT simulations of the electrochemical reactions of using P^3-S_x-P^3 structures as surrogate yield potential values in close agreement with the experimental results (see *SI Appendix*, Table S3 for the electrochemical potentials computed for a list of surrogate reactions as a function of x for both P_2S_5-Na_2S_x and Na_2S_x chemistry). The simulations confirm that as the S_x chain length reduces, the overall electrochemical potential also decreases. For x = 8, 6, and 4, evenly breaking the -S_x- chain in a P^3-S_x-P^3 structure has a higher potential value than breaking of the same chain unevenly. Moreover, the CV observations of the electrochemical activities as observed for both Na_2S_8 and P_2S_5-Na_2S_8 can be well explained by the DFT electrochemical potentials, summarized in Table 1. The assignment of the reactions in each activity regime is discussed in detail in *SI Appendix*, Section S2. Clearly, P_2S_5-Na_2S_8 has substantially more reactions involved in the electrochemical activities than Na_2S_8. For Na_2S_8, Na_2S_4, Na_2S_3, and Na_2S_2 are the key final products of its reduction. The lack of activities in CV below 1.6 V suggests that these products have low electrochemical activities even though all of them can be reduced further with electrochemical potentials ranging from 1.27 to 1.53 V. For the P_2S_5-Na_2S_8 complex, the initial reactions of P^3-S_8-P^3 favor the formation of shorted P^3-S_x-P^3 chains, thus producing probably a substantial amount of longer-chain Na_2S_x compounds as the reduction products. Most of them are known to be soluble in diglyme. The less soluble Na_2S_4 is probably coordinated with the complex in a mechanism similar to that shown in *SI Appendix*, Fig. S8. Regardless, an appreciable amount of the electrochemical activities is expected to be derived from the reduction of both Na_2S_x (x = 5, 6, and 7) and P^3-S_x-P^3 (x = 4, 5, 6, and 8).

Table 1. Reactions responsible for the major electrochemical activities*

	Na_2S_8	
Voltage observed†	2.2 V (major)	1.9 V (minor)
Reactions and DFT potentials	$Na_2S_8 \rightarrow Na_2S_4 + Na_2S_4$ (2.17 V) $Na_2S_8 \rightarrow Na_2S_3 + Na_2S_5$ (2.13 V)	$Na_2S_8 \rightarrow Na_2S_6 + Na_2S_2$ (1.86 V) $Na_2S_6 \rightarrow Na_2S_4 + Na_2S_2$ (1.85 V)
Voltage†	1.7 V (major)	
Reactions and DFT potentials	$Na_2S_5 \rightarrow Na_2S_3 + Na_2S_2$ (1.72 V)	
	P_2S_5-Na_2S_8	
Voltage observed†	2.23 V	2.11 V
Reactions and DFT potentials	P^3-S_8-$P^3 \rightarrow P^3$-S_4-$P^3 + Na_2S_4$ (2.24 V) **P^3-S_8-$P^3 \rightarrow P^3$-S_3-$P^3 + Na_2S_5$ (2.26 V)** P^3-S_8-$P^3 \rightarrow P^3$-S_2-$P^3 + Na_2S_6$ (2.27 V) P^3-S_8-$P^3 \rightarrow P^3$-S_1-$P^3 + Na_2S_7$ (2.21 V)	**P^3-S_8-$P^3 \rightarrow P^3$-S_5-$P^3 + Na_2S_3$ (2.11 V)** **P^3-S_5-$P^3 \rightarrow P^3$-S_2-$P^3 + Na_2S_3$ (2.07 V)** **P^3-S_4-$P^3 \rightarrow P^3$-S-$P^3 + Na_2S_3$ (2.09 V)** **$Na_2S_7 \rightarrow Na_2S_4 + Na_2S_3$ (2.12 V)**
Voltage observed†	1.93 V	1.70 V (and below)
Reactions and DFT potentials	P^3-S_8-$P^3 \rightarrow P^3$-S_6-$P^3 + Na_2S_2$ (1.89 V) P^3-S_6-$P^3 \rightarrow P^3$-S_4-$P^3 + Na_2S_2$ (1.89 V) **P^3-S_5-$P^3 \rightarrow P^3$-S_3-$P^3 + Na_2S_2$ (1.86 V)** $Na_2S_7 \rightarrow Na_2S_5 + Na_2S_2$ (1.94 V) $Na_2S_6 \rightarrow Na_2S_4 + Na_2S_2$ (1.85 V)	$Na_2S_5 \rightarrow Na_2S_3 + Na_2S_2$ (1.72 V) P^3-S_5-$P^3 \rightarrow P^3$-S_4-$P^3 + Na_2S$ (1.61 V) P^3-S_3-$P^3 \rightarrow P^3$-S_2-$P^3 + Na_2S$ (1.54 V) P^3-S_2-$P^3 \rightarrow P^3$-S-$P^3 + Na_2S$ (1.62 V)
	$\leftarrow P^3$-S_4-$P^3 \rightarrow P^3$-S_2-$P^3 + Na_2S_2$ (1.80 V) $\rightarrow$	

*See also *SI Appendix*, Table S3 for a wide range of the DFT potential values calculated. The reactions listed abbreviated. All reactions should be read as $Na_2S_x \xrightarrow{+2Na} Na_2S_{x-y} + Na_2S_y$ or P^3-S_x-$P^3 \xrightarrow{+2Na} P^3$-$S_{x-y}$-$P^3 + Na_2S_y$. The voltage values listed in parentheses are electrochemical potential values calculated at the UB3LYP/6–31 + G(2df,p) level of theory.

†Voltage at which intense electrochemical activities were experimentally observed.

Table 1 also reveals several other key mechanistic features. A substantial amount of the electrochemical activities above 1.8 V involves the production of $S_3^{\cdot-}$, i.e., P^3-S_3-P^3 and Na_2S_3 (bolded in the table). This is in agreement with the Raman observation discussed earlier; the discharge product detected at 1.8 V is mainly $S_3^{\cdot-}$. Also, the complex backbone structure is intact when discharged to 1.5–1.6 V. However, at and below about 1.7 V, we should see an increased production of Na_2S and hence an increased solid phase formation. For this reason, P_2S_5-Na_2S_8 is expected to give good cycle performance above 1.7 V, as will be demonstrated next. Also, the mechanism depicted in Fig. 2*A* is expected to be valid above the same voltage.

Performance Evaluation. To evaluate the cell electrochemical stability, galvanostatic cycling (Fig. 3*A*) was performed at 0.5C rate at room temperature and over the voltage range of 1.8–2.4 V, focusing on comparisons between a stoichiometric P_2S_5-Na_2S_8 and the reference Na_2S_8 catholyte paired with a passivated sodium metal anode. P_2S_5 itself does not yield any electrochemical activity, as shown in *SI Appendix*, Fig. S14. The key difference between the two cells, and hence with and without P_2S_5 complexation, is that over the above voltage range tested, the Na_2S_8 cell failed quickly, within 15 cycles at 1.8–2.4 V. In contrast, the P_2S_5-Na_2S_8 cells displays good cycling stability, sustained capacity retention, and excellent Coulombic efficiency (average value of ~95%) over 200 cycles. The less-than-ideal Coulombic efficiency (<99%) is due to parasitic reactions on the anode with the electrolyte over cycling. Also, cycling between 1.8 and 2.4 V, the P_2S_5-Na_2S_8 cell retains 80% of its capacity after 400 cycles (440 mAh g^{-1} initially versus 352 mAh g^{-1} after 400 cycles, both on an active sulfur basis). In addition, the higher capacity and discharge potential contribute to a higher energy density of 924 Wh kg^{-1} (calculated on the basis of 440 mAh g^{-1} × 2.10 V) than that of Na_2S_8 (682 Wh kg^{-1} calculated on the basis of 350 mAh g^{-1} × 1.95 V). At the lower (0.25) and higher (0.75) C-rates, the specific capacities measured were 460 and 380 mAh g^{-1}, respectively (Fig. 3*D*).

As with any battery chemistry, cell cycling stability decreases with excessive discharging. Repeated discharging of the P_2S_5-Na_2S_8 cell below 1.7 V is detrimental to cycle stability, as discussed before. Hence, while cycling to 1.2 V delivered a better initial capacity at 468 mAh g^{-1} on an active sulfur basis, the cell operated stably only for about 140 cycles, after which it exhibited a notable, albeit slow decay in capacity and Coulombic efficiency. The apparent increase in the capacity for the 1.2 V to 2.4 V cycling over the first 125 cycles is probably related to further molecular rearrangement of the complexes, which eventually deteriorates the performance. The decay is associated with the formation and accumulation of the electrochemically inactive discharge products such as Na_2S and Na_2S_2 that cannot be accommodated by the complex. These products resist electrochemical conversion back to the active P_2S_5-Na_2S_x ($x \geq 3$). Electrochemical impedance spectroscopy (Fig. 3*B*) shows that within 200 cycles, no obvious change is seen in the impedance profiles over 1.8 V to 2.4 V. When cycled to 1.2 V, however, the high-frequency impedance increases notably between 100 and 200 cycles. For the two characteristic impedance features observed for each case, the high-frequency mode reveals the interfacial resistance/capacitance of the catholyte, while the low-frequency mode is ascribed to the charge-transfer resistance/pseudocapacitance of the catholyte (21).

Scanning electron microscopy and energy-dispersive X-ray spectroscopy mappings offered definitive evidence that supports electrochemical stability of the P_2S_5-Na_2S_8 complex and the instability of Na_2S_8 in battery operations. The surface of the current collector dissembled from the P_2S_5-Na_2S_8 cell remains pristine after 30 cycles, with Na and S elements detected originating from soluble P_2S_5-Na_2S_x species absorbed by the current collector, while the electrode dissembled from the Na_2S_8 cell after the same number of cycles displays a large amount of solid precipitates or insoluble, low-order sodium polysulfides (Fig. 3*C*; *SI Appendix*, Fig. S16). The as-received current collector is shown in *SI Appendix*, Fig. S17.

The cycling stability is sensitive to the catholyte mass loading to an extent. In the range of catholyte material loading of 0.74 mg cm^{-2} to 1.57 mg cm^{-2}, the P_2S_5-Na_2S_8 cells exhibit steady cycling performance (Fig. 3*E*). At 2.08 and 2.25 mg cm^{-2}, however, capacity decay was observed (*SI Appendix*, Fig. S18). Further studies are needed to understand the sensitivity of cycling stability at high catholyte mass loadings.

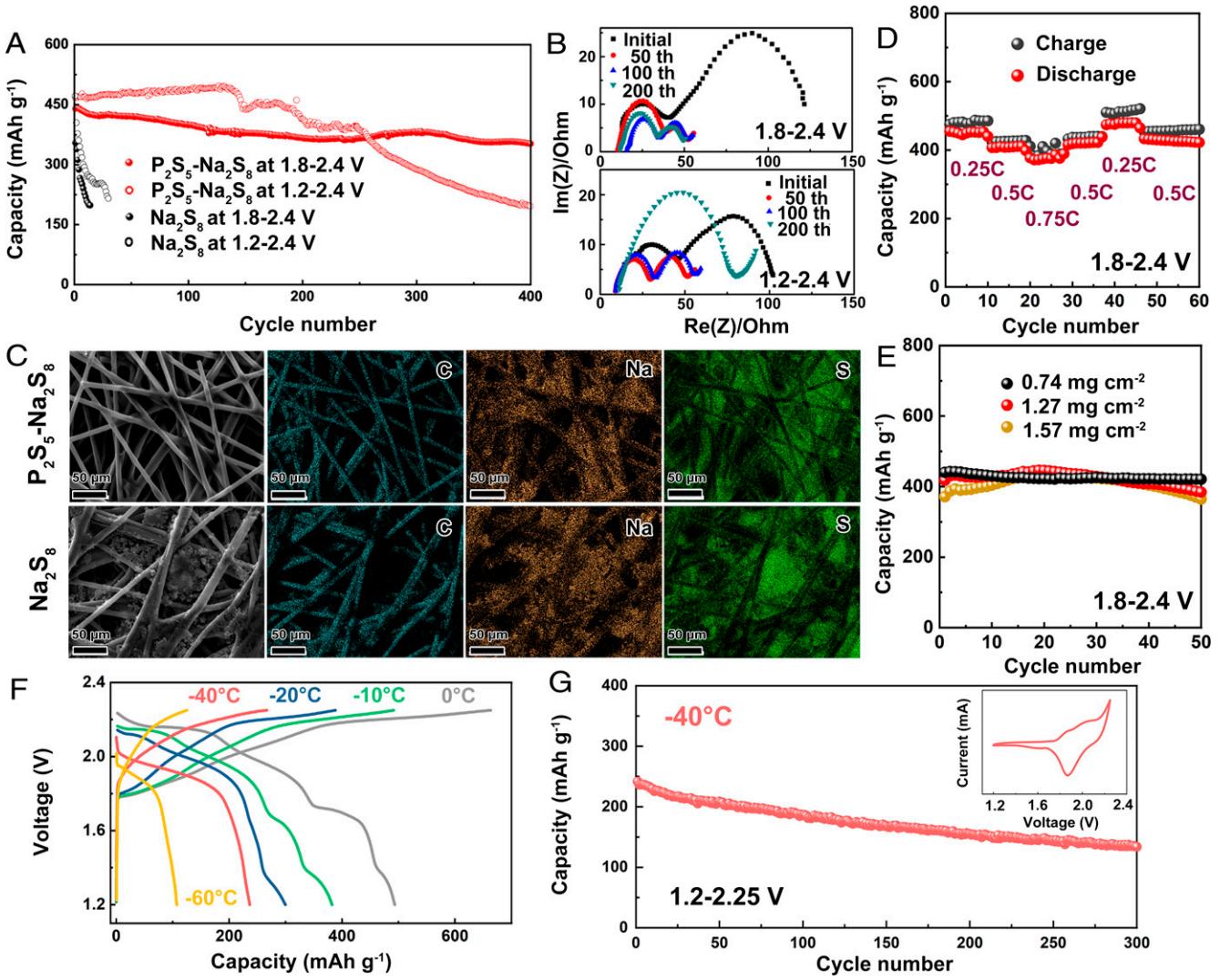

Fig. 3. Cell performance evaluation. (*A*) Galvanostatic cycling of the cells comparing P_2S_5-Na_2S_8 and Na_2S_8 as the catholytes at 0.5C (1C = 1,675 mA g^{-1}) at room temperature with voltage ranging from 1.8 V to 2.4 V and from 1.2 V to 2.4 V. The contrasts between the complexed system and noncomplexed systems are repeatable within cell-to-cell variations. (*B*) Electrochemical impedance spectroscopy on the P_2S_5-Na_2S_8 catholyte cells at room temperature before cycling and after 50, 100, or 200 cycles at 0.5C with voltage ranging from 1.8 V to 2.4 V and from 1.2 V to 2.4 V. (*C*) Scanning electron microscopy and corresponding elemental mappings of carbon, sodium and sulfur, comparing the P_2S_5-Na_2S_8 and Na_2S_8 catholyte current collectors after 30 cycles at the discharged state of 1.2 V. (*D*) Electrochemical cycling evaluation at different C-rates for a P_2S_5-Na_2S_8 catholyte cell, cycled between 1.8 V and 2.4 V. (*E*) Cycling performance of P_2S_5-Na_2S_8 catholytes over a range of active sulfur material loadings (up to 1.57 mg cm^{-2}). (*F*) Temperature-dependent galvanostatic charge-discharge voltage profiles of a P_2S_5-Na_2S_8 cell at 0.1C down to −60 °C with voltage cutoffs of 2.25 V and 1.2 V. (*G*) Long-term galvanostatic cycling of a P_2S_5-Na_2S_8 catholyte cell at 0.1C at −40 °C (*Inset*: CV profile at −40 °C).

A Randles–Sevcik analysis of the CV data shows that the Na^+ diffusion rates in the P_2S_5-Na_2S_8 cell are higher than the Na_2S_8 cell during both oxidation and reduction (*SI Appendix*, Fig. S11), suggesting that the P_2S_5-Na_2S_8 cell should also give reasonably good performance at reduced temperatures. Indeed, the charge-discharge profiles collected at 0, −10, −20, −40, and −60 °C (Fig. 3*F*) show that at the 0.1C rate tested, although the initial discharge capacity decreases sequentially with a decrease in temperature (493, 382, 300, 237, and 107 mAh per gram of active sulfur at 0, −10, −20, −40, and −60 °C, respectively), the cell is operational even at −60 °C. It retains 55.4% of the initial capacity over 300 cycles at −40 °C (242 mAh g^{-1} initially) (Fig. 3*G*). The inset of Fig. 3*G* shows that at −40 °C, redox peaks are still visible. These results indicate a further advantage associated with the complexation, as it offers a key solution to overcoming the reaction kinetic barriers that are inherent to the traditional Na-S electrochemistry.

Discussion and Conclusions

We propose here a series of sodium phosphorothioate (mP_2S_5-nNa_2S_x) complexes as promising cathode materials for sodium batteries. We show that the complexation is a viable approach to reducing cyclic liquid–solid phase transitions in sodium-sulfur batteries. After exploring and tuning the S_x chain length for the stoichiometric P_2S_5/Na_2S_x ratio, we demonstrate that at room temperature and as a catholyte, the P_2S_5-Na_2S_8 complex maintained excellent capacity retention (80% over 400 cycles) and Coulombic efficiency (>95% over 200 cycles) without having to sacrifice storage capacity significantly on the basis of complex material mass. The improved electrochemical reaction kinetics extends the cell operability to reduced temperatures (down to −60 °C tested) with long-term operability at −40 °C. The structures of the complexes, the complexation mechanisms, and the associated electrochemical reaction mechanisms are proposed on the basis of comprehensive

Raman and NMR characterizations and DFT calculations. The analyses suggest that complexation provides a hosting molecular structure that anchors and stores discharged products that would otherwise precipitate out of the solvent. The complexation also enhances the electrochemical potential and Na^+ ion conductivity. With the additional dimension in the molar P_2S_5/Na_2S_x ratios that are yet to be explored, it is possible that the mP_2S_5-nNa_2S_x complexes present additional attractive properties as a suitable sodium-sulfur battery cathode material.

Materials and Methods

Details of the materials, chemicals, and methods used in this work, including complexes preparation, catholyte preparation, sodium metal anode passivation, coin-cell type, separator, electrochemical measurements, material characterizations, and DFT calculations, are provided in *SI Appendix, Methods*.

Data Availability. All study data are included in the manuscript and/or *SI Appendix*.

ACKNOWLEDGMENTS We acknowledge the assistance of Dr. Min Li, Prof. Hailiang Wang, Yiren Zhong, and Zishan Wu for X-ray photoelectron spectroscopy (XPS) characterization. We also acknowledge the assistance of Jean Carlan for NMR characterization. W.L. acknowledges the support from the Young Investigator Program funded by US Air Force Office of Scientific Research (AFOSR) under award FA9550-17-1-0184, which supports the initial discovery of the idea. W.L. also acknowledges the support from the Young Investigator Program funded by NASA's Space Technology Research Grants Program under award 80NSSC18K1514, which further supports on the project. H.W. acknowledges the partial support by US AFOSR under Grants FA9550-19-1-0261 and FA9550-16-1-0195. J.C. is partially supported by the NSF Graduate Research Fellowship Grant DGE-1656518.

1. B. Dunn, H. Kamath, J.-M. Tarascon, Electrical energy storage for the grid: A battery of choices. *Science* **334**, 928–935 (2011).
2. N. Yabuuchi, K. Kubota, M. Dahbi, S. Komaba, Research development on sodium-ion batteries. *Chem. Rev.* **114**, 11636–11682 (2014).
3. K. Chayambuka, G. Mulder, D. Danilov, P. Notten, Sodium-ion battery materials and electrochemical properties reviewed. *Adv. Energy Mater.* **8**, 1800079 (2018).
4. Y. Zhao, K. Adair, X. Sun, Recent developments and insights into the understanding of Na metal anodes for Na-metal batteries. *Energy Environ. Sci.* **11**, 2673–2695 (2018).
5. P. Adelhelm *et al.*, From lithium to sodium: Cell chemistry of room temperature sodium-air and sodium-sulfur batteries. *Beilstein J. Nanotechnol.* **6**, 1016–1055 (2015).
6. A. Manthiram, X. Yu, Ambient temperature sodium-sulfur batteries. *small* **11**, 2108–2114 (2015).
7. S. Wei *et al.*, A stable room-temperature sodium-sulfur battery. *Nat. Commun.* **7**, 11722 (2016).
8. B.-W. Zhang *et al.*, Atomic cobalt as an efficient electrocatalyst in sulfur cathodes for superior room-temperature sodium-sulfur batteries. *Nat. Commun.* **9**, 4082 (2018).
9. X. Xu *et al.*, A room-temperature sodium-sulfur battery with high capacity and stable cycling performance. *Nat. Commun.* **9**, 3870 (2018).
10. R. Chen, R. Luo, Y. Huang, F. Wu, L. Li, Advanced high energy density secondary batteries with multi-electron reaction materials. *Adv. Sci. (Weinh.)* **3**, 1600051 (2016).
11. Y.-X. Wang *et al.*, Room-temperature sodium-sulfur batteries: A comprehensive review on research progress and cell chemistry. *Adv. Energy Mater.* **7**, 1602829 (2017).
12. A. Eng *et al.*, Room-temperature sodium-sulfur batteries and beyond: Realizing practical high energy systems through anode, cathode, and electrolyte engineering. *Adv. Energy Mater.* **11**, 2003493 (2021).
13. C. Wang *et al.*, Frogspawn-coral-like hollow sodium sulfide nanostructured cathode for high-rate performance sodium–sulfur batteries. *Adv. Energy Mater.* **9**, 1803251 (2019).
14. C. Bischoff, K. Schuller, M. Haynes, S. W. Martin, Structural investigations of $yNa_2S + (1-y)\ PS_{5/2}$ glasses using Raman and infrared spectroscopies. *J. Non-Cryst. Solids* **358**, 3216–3222 (2012).
15. D. E. Watson, S. W. Martin, Structural characterization of the short-range order in high alkali content sodium thiosilicophosphate glasses. *Inorg. Chem.* **57**, 72–81 (2018).
16. C. Bischoff, K. Schuller, N. Dunlap, S. W. Martin, IR, Raman, and NMR studies of the short-range structures of $0.5Na_2S + 0.5[xGeS_2 + (1\text{-}x)PS_{5/2}]$ mixed glass-former glasses. *J. Phys. Chem. B* **118**, 1943–1953 (2014).
17. C. Dietrich *et al.*, Synthesis, structural characterization, and lithium ion conductivity of the lithium thioposphate $Li_2P_2S_6$. *Inorg. Chem.* **56**, 6681–6687 (2017).
18. J. Pernert, J. Brown, Some reactions and properties of the phosphorus sulfides. *Chem. Eng. News* **27**, 2143–2145 (1949).
19. Q. Pang, X. Liang, A. Shyamsunder, L. F. Nazar, An in vivo formed solid electrolyte surface layer enables stable plating of Li metal. *Joule* **1**, 1–16 (2017).
20. D. A. Ziolkowska, W. Arnold, T. Druffel, M. Sunkara, H. Wang, Rapid and economic synthesis of a Li_7PS_6 solid electrolyte from a liquid approach. *ACS Appl. Mater. Interfaces* **11**, 6015–6021 (2019).
21. H. Chen *et al.*, Sulphur-impregnated flow cathode to enable high-energy-density lithium flow batteries. *Nat. Commun.* **6**, 5877 (2015).